

Orthogonal interlayer coupling in an all-antiferromagnetic junction

Yongjian Zhou

Tsinghua University

Liyang Liao

Tsinghua University

Tingwen Guo

Tsinghua University

Hua Bai

Tsinghua University

Mingkun Zhao

Institute of Physics, Chinese Academy of Sciences

Cai-Hua Wan

Chinese Academy of Sciences

Lin Huang

Tsinghua University

Lei Han

Tsinghua University

Ruyi Chen

Tsinghua University

Zhiyuan Zhou

Tsinghua University

Xiufeng Han

Beijing National Laboratory for Condensed Matter Physics, Institute of Physics, University of Chinese Academy of Sciences, Chinese Academy of Sciences, Beijing 100190, China <https://orcid.org/0000-0001-8053-793X>

Feng Pan

Tsinghua University

Cheng Song (✉ songcheng@mail.tsinghua.edu.cn)

Tsinghua University <https://orcid.org/0000-0002-7651-9031>

Article

Keywords: antiferromagnets (AFMs), interlayer coupling, orthogonal interlayer coupling

Posted Date: November 19th, 2021

DOI: <https://doi.org/10.21203/rs.3.rs-882829/v1>

License:  This work is licensed under a Creative Commons Attribution 4.0 International License.

[Read Full License](#)

Version of Record: A version of this preprint was published at Nature Communications on June 28th, 2022. See the published version at <https://doi.org/10.1038/s41467-022-31531-w>.

Abstract

The interlayer coupling of two ferromagnetic layers results in found of giant magnetoresistance, which forms the foundation of spintronics and accelerates the development of information technology. Compared with ferromagnets, antiferromagnets (AFMs) possess huge potential in ultrafast and high-density data processing and information storage because of their terahertz spin dynamics and subtle stray field. The interlayer coupling in AFMs has long been neglected, because the collinear parallel and antiparallel arrangements of AFMs are indistinguishable. However, the noncollinear interlayer coupling in AFMs is detectable, and can be a potential candidate for practical antiferromagnetic spintronic devices. Here we demonstrate orthogonal interlayer coupling at room temperature in an all-antiferromagnetic junction $\text{Fe}_2\text{O}_3/\text{Cr}_2\text{O}_3/\text{Fe}_2\text{O}_3$, where the Néel vectors in the top and bottom functional materials Fe_2O_3 are strongly orthogonally coupled and the coupling strength of which is significantly affected by the thickness of the antiferromagnetic Cr_2O_3 spacer. From the energy and symmetry analysis, the direct coupling via uniform magnetic ordering is excluded. The coupling is proposed to be mediated by quasi-long range order in the spacer. Besides the fundamental significance, the strong coupling in an antiferromagnetic junction makes it a promising building block for practical antiferromagnetic spintronics with high-speed operation and ultrahigh-density integration.

Main Text

The found of interlayer coupling between two separated magnetic layers brings innovations and new development opportunities to the microelectronics industry¹. The most well-established interlayer coupling, known as Ruderman-Kittel-Kasuya-Yosida (RKKY) interaction², leads to parallel and antiparallel alignment of magnetizations in two ferromagnets (FM1 and FM2) separated by a non-magnetic spacer (Fig. 1a) which results in the discovery of giant magnetoresistance (GMR)³⁻⁵, boom of the field of spintronics and the consequent revolution of information storage^{1,6}. Nevertheless, the ferromagnets have drawbacks such as large stray field which is destructive for the tightly packed devices, and the intrinsic gigahertz frequency which limits the fundamental operating speed of FM system. Antiferromagnets (AFMs) are promising candidates for solving these problems and for the next generation of spintronics because of the subtle net moment which eliminates operation cross-talk^{7,8}, and extremely high eigenfrequency up to terahertz⁹⁻¹². The interlayer coupling of AFMs has been overlooked because the collinear parallel and antiparallel arrangements are indiscernible and useless for application, since most antiferromagnets could be seen as having symmetry macroscopically at zero field. However, noncollinear such as orthogonal interlayer coupling of AFMs can be possibly detected and is meaningful for antiferromagnetic spintronics/magnonics related to the relative direction of Néel vectors¹³. Such a noncollinear interlayer coupling remains elusive.

The absence of net moment and insensitiveness to magnetic field pose a tremendous challenge on unravelling antiferromagnetic interlayer coupling. As a pioneering work, it is highly significant to use AFM with Néel vectors that are accessible to control and readout for the coupling layers. $\alpha\text{-Fe}_2\text{O}_3$ is a high-

Néel-temperature antiferromagnet¹⁴ with a weak in-plane anisotropy and concomitant low spin-flop field^{15,16}, as well as sizable spin Hall magnetoresistance (SMR) signals to record its Néel vector¹⁷⁻²¹. Here, we demonstrate unprecedented orthogonal coupling of Néel vectors (Fig. 1b) between two antiferromagnetic α -Fe₂O₃ layers in a Fe₂O₃/Cr₂O₃/Fe₂O₃ junction via magneto-transport measurements and x-ray magnetic linear dichroism (XMLD) spectra. The coupling can be mediated by quasi-long range order in the Cr₂O₃ spacer, which is supported by our theory model. Interlayer coupling effect via direct uniform magnetic ordering is excluded by the energy and symmetry analysis. The interlayer coupling in an all-antiferromagnetic junction makes it a promising candidate building block for practical antiferromagnetic spintronics²²⁻²⁶ and magnonics^{15,27,28}, which have attracted increasing attention because of their potential applications on ultrahigh-density information storage and high-frequency devices^{7,29,30}.

Results

SMR and XMLD measurements. We first show in Fig. 2a SMR signals of a control sample Fe₂O₃(12)/Pt(4) (units in nanometers), where the magnetic field (H) and current (I) is along x -axis and the spin polarization generated by the spin Hall effect of Pt is along y -axis. As expected, comparatively low resistance states at high magnetic fields reflect that the Néel vector (n) of Fe₂O₃ is perpendicular to $H(I)$ due to the spin-flop at high fields and deviates towards $H(I)$ at low fields, which is quite characteristic for negative SMR of AFM¹⁷⁻²⁰. The resistance peaks at approximately $\mu_0 H = \pm 0.35$ T owing to the deviation of n from the spin-flop state appears at a negative field as sweeping the field from positive to negative (black line), indicating that the Néel vector almost keeps the spin-flop state at zero-field¹⁶. Note that Fe₂O₃ with the thickness below tens of nanometers maintains easy-plane anisotropy without Morin transition^{16,18,20}. Similar SMR signals are obtained in another control sample Cr₂O₃(4.4)/Fe₂O₃(4)/Pt(4) (Fig. 2b), where Fe₂O₃ was grown on a Cr₂O₃ buffer to ensure a closer scenario as the top Fe₂O₃ in the Fe₂O₃/Cr₂O₃/Fe₂O₃ junction. The SMR signals of the control samples are simulated and shown in Supplementary Note 2, where the hysteresis is due to the existence of Dzyaloshinskii-Moriya interaction (DMI) in Fe₂O₃³¹. The antiferromagnetic Cr₂O₃ buffer possesses a high spin-flop field higher than 6 T⁹, which does not contribute to the observed SMR signals.

Figure 2c displays a representative HAADF-STEM (high-angle annular dark-field scanning transmission electron microscopy) image of the Fe₂O₃(12)/Cr₂O₃(4.4)/Fe₂O₃(4) cross-section, reflecting the epitaxial growth of the junction (Supplementary Note 3). Figure 2d presents the SMR curves of the Fe₂O₃/Cr₂O₃/Fe₂O₃ junction, which was covered by 4 nm-thick Pt. Four typical $H[(i) \rightarrow (iv)]$ are denoted in the inset. The most eminent feature is that two resistance peaks exist when sweeping H from positive to negative (black line) or reverse (red line), which is different from the SMR signals of a single Fe₂O₃ in Fig. 2a,b. The resistance peak appears before $H = 0$, which violates the principle of thermodynamics, indicating the existences of coupling effect. A low resistance is obtained for $n \perp I$ (n is parallel to spin polarization) at the spin-flop state. As H is swept downward, the first resistance peak (high resistance

state) at a positive H [$\mu_0 H = +0.3$ T, (i)] reveals that n deviates from the spin-flop state and is unexpectedly aligned along $n // H(l)$. This observation indicates that another effect suppresses the magnetic field effect. We attribute the overwhelming effect to the interlayer coupling between two Fe_2O_3 layers through the Cr_2O_3 spacer. The AFM coupling generates an orthogonal (90°) arrangement of n in two Fe_2O_3 layers. The coupling between net moment in Cr_2O_3 at high temperature and n in Fe_2O_3 is excluded (Supplementary Note 4). Based on both magnetic field (Fig. 2a,b) and angle dependent SMR measurements (Supplementary Note 5) in $\text{Fe}_2\text{O}_3/\text{Pt}$ and $\text{Cr}_2\text{O}_3/\text{Fe}_2\text{O}_3/\text{Pt}$ control samples, we find the top thinner Fe_2O_3 possesses a lower spin-flop field than its bottom thicker counterpart, in analogy to a soft ferromagnet with a small coercivity. Because of the relatively lower spin-flop field and smaller Zeeman energy of top thinner Fe_2O_3 , the n in the top Fe_2O_3 has the priority to deviate from the spin-flop state as a result of the interlayer coupling, resulting in the resistance peak before zero-field. This is bolstered by the simulation based on calculating the energy profile of different magnetic configurations in Fig. 2e (Supplementary Note 2).

As H sweeps to the negative side, the SMR signal decreases and a resistance valley appears at negative H (ii), which is almost the same as the location of resistance peak in Fig. 2a. The direction of n in the bottom Fe_2O_3 is $n // H$, and the interlayer coupling drives the Néel vector in the top Fe_2O_3 to $n \perp H(l)$, again giving rise to the orthogonal configuration [(ii)' in Fig. 2e]. In this case, the spin current is reflected at the interface between Pt/top Fe_2O_3 , leading to the relatively low resistance. The SMR valley in $\text{Fe}_2\text{O}_3/\text{Cr}_2\text{O}_3/\text{Fe}_2\text{O}_3$ occurs at the magnetic field that is much larger than that of net moment reversal (Supplementary Note 6), excluding possible coupling between net moment in Cr_2O_3 at high temperature and n in Fe_2O_3 as well as artifacts due to positive SMR from weak ferromagnetism (caused by defects or uncompensated interface). Then n in the bottom Fe_2O_3 rotates towards the spin-flop state ($n \perp H$) due to the increasing negative H , and n in the top Fe_2O_3 deviates towards $n // H(l)$ [(iii)' in Fig. 2e], resulting in the absorption of spin current and the second resistance peak (iii). It should be clarified that the second peak can exist when the coupling energy is large enough to overcome the Zeeman energy of the top Fe_2O_3 at the valley (ii), otherwise the n (top Fe_2O_3) will maintain spin-flop state rather than deviating towards $n // H$. The magnitude of the second peak is smaller than the first one can be ascribed to less component of n along x -axis. In contrast, the SMR in inverted sandwich, $\text{Fe}_2\text{O}_3(4)/\text{Cr}_2\text{O}_3(4.4)/\text{Fe}_2\text{O}_3(12)$ (Supplementary Note 7), does not present resistance peak signal before $H = 0$, demonstrating that the n in the 12 nm-thick Fe_2O_3 maintains spin-flop state rather than deviating towards H at low magnetic field because of the large Zeeman energy, indicating the existence of the orthogonal coupling.

Besides magneto-transport measurements, we further confirm the interlayer coupling by direct Néel vector characterizations. Fe L -edge XMLD spectra were used to detect the n of the top Fe_2O_3 (several nanometers-thick sensitivity) in the $\text{Fe}_2\text{O}_3/\text{Cr}_2\text{O}_3/\text{Fe}_2\text{O}_3$ junction, where 2 nm-thick Pt was deposited on top. The XMLD spectra were recorded at zero-field after applying a high magnetic field along the x -axis for the sake of the non-volatile feature of n in easy-plane Fe_2O_3 ¹⁶. X-ray was vertically incident to the film and the polarized direction was parallel to the film plane. XMLD signals are obtained as $\text{XMLD} = \text{XAS}_{\perp} -$

XAS_{//}, where XAS_{//} and XAS_⊥ denote the x-ray absorption spectroscopy (XAS) recorded with polarization parallel with x -axis ($//$) and y -axis (\perp), respectively. Corresponding data are presented in Fig. 2f, where L_2 -edge is highlighted because it is generally used for the Fe-based XMLD spectra analysis^{32,33}. Remarkably, Fe L_2 -edge XMLD spectrum exhibits a zero–positive–negative–zero feature, which is quite a characteristic for the n along the parallel direction ($n // x$ -axis)^{32,33}, rather than the spin-flop direction (y -axis). The n (top Fe₂O₃) aligned along H confirms the interlayer coupling, which is also corroborated by a series of XMLD measurements with sample rotation (Supplementary Note 8). The scenarios differ dramatically for the control samples Fe₂O₃ and Cr₂O₃/Fe₂O₃, in which identical experiments were carried out, but an opposite polarity at L_2 -edge (Fig. 2g,h, respectively), namely zero–negative–positive–zero, was observed, suggesting that the n in Fe₂O₃ is mainly aligned along the spin-flop direction ($n // y$ -axis) without interlayer coupling.

Temperature dependence of interlayer coupling. We now turn towards the temperature dependence of SMR measurements in Fe₂O₃/Cr₂O₃/Fe₂O₃/Pt samples. Figure 3a shows the SMR results at various temperatures (Supplementary Note 9). At a relatively high temperature ($T = 270$ K), there exists two resistance peaks as we discussed above for $T = 300$ K, but the intensity of the second peak is lower than that at $T = 300$ K. Such a tendency continues with further decreasing temperature to 250 K, producing a tiny peak (or just a protruding), accompanied by the absence the second peak at 200 K. Also visible is that the location of the first resistance peak shifts towards zero-field with decreasing T but maintains at positive H , reflecting $n // H$ in the top Fe₂O₃ before zero-field. This behavior discloses that although the interlayer coupling persists at low temperatures, the coupling energy decreases, resulting in the dominant spin-flop state and the disappearance of the second resistance peak. This phenomenon is similar to the temperature dependence of the spin fluctuation around equilibrium position in Cr₂O₃ spacer¹³. And we also demonstrate that the interlayer coupling does not depend on the magnetic field direction and the magnitude of applied reading current (Supplementary Note 10 and 11).

In addition to the H -dependent SMR we have explored the interlayer coupling between antiferromagnets by in-plane angle(α)-dependent SMR. Corresponding data of the Fe₂O₃/Cr₂O₃/Fe₂O₃/Pt sample at $T = 300$ K measured at two typical field of 0.5 T and 1 T are shown in Fig. 3b where $\alpha = 0^\circ$ means $H // l$. For $\mu_0 H = 1$ T, the SMR signals exhibit a negative polarity with the valley at $\alpha = 0^\circ$, which is a typical feature for the antiferromagnetic SMR at spin-flop state^{18,19}. The situation differs dramatically for $\mu_0 H = 0.5$ T. The SMR curve exhibits a positive polarity, indicating that the Néel vector of the top Fe₂O₃ maintains $n // H$ due to the dominant interlayer coupling. This finding coincides with the results of field dependent SMR. In contrast, the polarity of SMR keeps negative in the control sample Cr₂O₃/Fe₂O₃/Pt (Supplementary Note 4), reflecting the antiferromagnetic feature of Fe₂O₃ and the absence of the interlayer coupling. Identical angle-dependent measurements were carried out in the Fe₂O₃/Cr₂O₃/Fe₂O₃/Pt sample with $\mu_0 H = 0.5$ T at various temperatures. The polarity of SMR is positive at high temperatures ($T = 350$ and 300 K). With decreasing temperature to 250 K, the SMR signals become quite weak or even noisy, because of a competition between the interlayer coupling ($n // H$) and the H -induced spin-flop ($n \perp H$). This is

accompanied by the typically negative SMR induced by the spin-flop with further decreasing temperature to 230 K and 200 K. The polarity of the control sample Cr₂O₃/Fe₂O₃/Pt is always negative at different temperatures (Supplementary Note 4), reflecting the absence of the interlayer coupling and further eliminating the existences of coupling between net moment in Cr₂O₃ and Néel vectors in top Fe₂O₃.

Interlayer coupling strength. It is significant to characterize the interlayer coupling strength. Considering that the existence of the first peak is the compromise between the interlayer coupling and spin-flop state, its location ($\mu_0 H_{\text{Coupling}}$) as a function of temperature for different Cr₂O₃ thicknesses (t) is summarized in Fig. 4a (Supplementary Note 12) to reflect the coupling strength. The first peak persists at a positive field for all of the measured SMR curves, suggesting the orthogonal antiferromagnetic interlayer coupling when the t ranges 3–4.4 nm. The maximum coupling strength increases with decreasing Cr₂O₃ thickness. For thin Cr₂O₃ ($t = 3.0$ and 3.5 nm), $\mu_0 H_{\text{Coupling}}$ emerges from about 10 K, increases with increasing temperature and gets saturated at around 150 K. A plateau of the coupling strength exists from 150 K to 300 K. Then the coupling strength drops just above room temperature, which coincides with the spin fluctuation in Cr₂O₃ (bulk Néel temperature ~ 307 K)¹³. While for thick Cr₂O₃ ($t = 4.1$ and 4.4 nm), $\mu_0 H_{\text{Coupling}}$ has an onset temperature of about 100 K, increases with increasing temperature and reaches the maximum just above room temperature, then drops, without showing a plateau. For thicker Cr₂O₃ ($t = 6$ and 12 nm), Fe₂O₃/Cr₂O₃/Fe₂O₃/Pt samples show almost the same SMR signals at 300 K as samples with only one Fe₂O₃ layer (Supplementary Note 13), indicating the absence of the interlayer coupling when the Cr₂O₃ layer is too thick. In addition, the interlayer coupling is observed in the Fe₂O₃/NiO/Fe₂O₃ junction with antiferromagnetic NiO spacer (Supplementary Note 14), indicating that the coupling effect is not restricted to a certain spaced material.

The distinct behavior for the samples with thin and thick Cr₂O₃ shows a significant role of spacer thickness. Since the out-of-plane anisotropy decrease rapidly with smaller sample size³⁴, the most possible origin of the two distinct types of temperature dependence is that at low temperature, the moments in the thin Cr₂O₃ already have large in-plane component^{34–37}, but the thick Cr₂O₃ have stable out-of-plane Néel order. The coupling arises from the fluctuating magnetic moments, hence thin Cr₂O₃ mediates coupling in low temperature, and thick Cr₂O₃ can only mediate coupling above 100 K.

As the coupling field shifts towards $H = 0$ with decreasing temperature, the magnitude of second resistance peak, which is also related to the deviation of Néel vector in top Fe₂O₃, also changes (Fig. 3a). We then summarize in Fig. 4b the temperature dependent magnetoresistance (MR) for the Fe₂O₃/Cr₂O₃/Fe₂O₃/Pt samples with various t . MR is related to the magnitude of the second resistance peak and is defined as $MR = [R(\text{second peak}) - R(\text{lowest})]/R(\text{lowest})$, where the lowest is the minimum of the SMR curves. It can be seen that the MR exhibits a similar temperature dependence as the coupling field, strongly suggesting that the MR is also relevant to the interlayer coupling. As we discussed above (Fig. 2d), the second resistance peak is the result of competition between interlayer coupling and spin-flop state in the top Fe₂O₃ at the valley. When the temperature is low, the coupling energy is relatively small as

compared with the Zeeman energy. Therefore, the Néel vector in the top Fe_2O_3 maintains spin-flop state ($n \perp H$), causing the vanishment of the second peak. The vanishing temperature (MR = 0) is obviously higher than its counterpart for no coupling effect ($\mu_0 H_{\text{Coupling}} = 0$), such as $T = 225$ K and $T = 125$ K for $t = 4.4$ nm, respectively. With further increase of temperature, the coupling energy is enhanced and exceeds the Zeeman energy, resulting in the deviation of more n towards H and the resultant rapid rise of the second resistance peak (MR). As the spin correlation is partially destroyed at high temperatures ($T > 340$ K for $t = 4.4$ nm), the coupling is reduced, accompanied by the decreasing of MR. An analogical situation occurs for the other samples ($t = 3.0, 3.5,$ and 4.1 nm), while the samples with thin ($t = 3.0$ and 3.5 nm) and thick ($t = 4.1$ and 4.4 nm) Cr_2O_3 are divided into two groups according to the temperature dependence of the coupling strength.

Analysis on the magnetic ordering. In the following we discuss the role of magnetic ordering in the Cr_2O_3 spacer in the interlayer coupling of Fe_2O_3 . The energies related to the Cr_2O_3 magnetic ordering are the interfacial coupling $F(\mathbf{N}_{t,\text{Fe}}, \mathbf{M}_{t,\text{Fe}}, \mathbf{N}_{t,\text{Cr}}, \mathbf{M}_{t,\text{Cr}})$, $F(\mathbf{N}_{b,\text{Fe}}, \mathbf{M}_{b,\text{Fe}}, \mathbf{N}_{b,\text{Cr}}, \mathbf{M}_{b,\text{Cr}})$, and the magnetic energy U in the Cr_2O_3 spacer, where \mathbf{N} is the Néel vector and \mathbf{M} is the net magnetization, t, b label the top and bottom surfaces, respectively. For thinner sample, the exchange energy makes it harder to let $(\mathbf{N}_{t,\text{Cr}}, \mathbf{M}_{t,\text{Cr}}) \neq (\mathbf{N}_{b,\text{Cr}}, \mathbf{M}_{b,\text{Cr}})$. Thus, the observed interlayer coupling which increases with decreasing Cr_2O_3 thickness is hard to be explained by the non-uniform distribution of the magnetic order in Cr_2O_3 in the thickness direction. Also, it is known that Cr_2O_3 is lack of inter-unit cell DMI³¹, which favor out-of-plane spiral spin structure and may cause $(\mathbf{N}_{t,\text{Cr}}, \mathbf{M}_{t,\text{Cr}}) \neq (\mathbf{N}_{b,\text{Cr}}, \mathbf{M}_{b,\text{Cr}})$. If $(\mathbf{N}_{t,\text{Cr}}, \mathbf{M}_{t,\text{Cr}}) = (\mathbf{N}_{b,\text{Cr}}, \mathbf{M}_{b,\text{Cr}})$, assuming $F(\mathbf{N}_{t,\text{Fe}}, \mathbf{M}_{t,\text{Fe}}, \mathbf{N}_{t,\text{Cr}}, \mathbf{M}_{t,\text{Cr}}) \leq F(\mathbf{N}_{b,\text{Fe}}, \mathbf{M}_{b,\text{Fe}}, \mathbf{N}_{b,\text{Cr}}, \mathbf{M}_{b,\text{Cr}})$, one can lower the total energy by rotating $(\mathbf{N}_{b,\text{Fe}}, \mathbf{M}_{b,\text{Fe}})$ towards $(\mathbf{N}_{t,\text{Fe}}, \mathbf{M}_{t,\text{Fe}})$. The process above is solid even when the interfacial coupling at different interfaces has a different magnitude, as long as the interfacial coupling has the same form. Thus, by considering the Cr_2O_3 magnetic ordering which is uniform in the film plane, the lowest energy state always has $(\mathbf{N}_{b,\text{Fe}}, \mathbf{M}_{b,\text{Fe}}) = (\mathbf{N}_{t,\text{Fe}}, \mathbf{M}_{t,\text{Fe}})$, i.e., no orthogonal interlayer coupling can be generated.

Quasi-long range order mediated interlayer coupling. Having excluded the magnetic ordering which is uniform in the film plane as the origin of the interlayer coupling, we thus consider magnetic ordering which is non-uniform in the film plane, i.e., quasi-long range order (QLRO) enabled by fluctuations. It is known that in extremely thin magnets with in-plane moments, long-range magnetic order could be absent easily³⁸, while spin correlation still exists³⁹, which distinguishes from disorder paramagnetic phase [Fig. 4(e)]. Indeed, such QLRO emerges when the film gets thinner and the system drops from three to two dimension, consistent with the larger coupling strength in thinner films. Meanwhile, the temperature-dependent behavior of $\mu_0 H_{\text{Coupling}}$ in Fig. 4a also strongly suggests that the interlayer coupling is correlated to the spin fluctuation in the Cr_2O_3 spacer. For QLRO state in the Cr_2O_3 sandwiched by two Fe_2O_3 layers, the parallel and perpendicular arrangements of the n in the two Fe_2O_3 layers means different boundary conditions. The perpendicular arrangement provides potential with D_{2d} symmetry for QLRO rather than the D_{2h} symmetry in parallel arrangement condition. Since the in-plane component of the moments point to all in-plane directions in QLRO state, the perpendicular arrangement provides more

symmetric environment for such excitations than the parallel arrangement. Hence, we assume a smaller energy in the perpendicular arrangement, with the same entropy in the two arrangements since the entropy only depends on the QLRO itself⁴⁰. This smaller energy makes the perpendicular arrangement favorable in the free energy, leading to the orthogonal interlayer coupling in the QLRO state.

Based on the above considerations, the schematic free energy diagrams at zero field for the thin and thick Cr₂O₃ cases are shown in Fig. 4(c) and (d), respectively. The ordered ground state has a free energy of F_0 , and all other states are represented by their free energy difference with the ground state $F - F_0$. In thin Cr₂O₃ cases, no coupling exists in the ground state. At T_1 , QLRO emerges under the perpendicular condition, while the Cr₂O₃ under the parallel condition remains in the ground state. Therefore, the coupling emerges with a coupling strength represented by $F_0 - F(\text{QLRO}@90^\circ)$ and increasing from T_1 to T_2 . At T_2 , the Cr₂O₃ under the parallel condition switches from the ground state to the QLRO state, and the coupling strength saturates to $F(\text{QLRO}@0^\circ) - F(\text{QLRO}@90^\circ)$. Then the Cr₂O₃ under the parallel condition switches from the QLRO state to paramagnetic state at T_3 , and the coupling strength $F(\text{paramagnet}) - F(\text{QLRO}@90^\circ)$ starts to decrease. The coupling strength finally vanishes at T_4 , where the Cr₂O₃ under the perpendicular condition switches to the disorder paramagnetic phase. Similar process happens to the thick Cr₂O₃ cases, with a larger T_1 because the perpendicular anisotropy stabilizes the Néel order in the ground state. The coupling strength increases up to T_3^* , where the Cr₂O₃ under the parallel condition switches from the ground state directly to the disorder state, without entering the QLRO state. Then the coupling strength decreases and finally vanishes at T_4 .

The phase transition from the ordered ground state to the QLRO state can be phenomenally described by the following free energy

$$F = (\Delta - \lambda T)q + bn^4 \quad (1)$$

where T is the temperature, b is a parameter to stabilize the Néel Order, and λ is a parameter related to the entropy difference between the ground state and the QLRO. Δ reflects the energy difference between the ground state and the QLRO, with values Δ_\perp and Δ_\parallel for the perpendicular and the parallel conditions, respectively. Δ_\perp is smaller than Δ_\parallel and $\Delta_\parallel - \Delta_\perp$ increases with decreasing Cr₂O₃ thickness. The Néel Order n and the volume of the QLRO state q satisfies

$$q + n^2 = 1 \quad (2)$$

The first term in (1) describes the blue and red lines in Fig.4(c) and (d), and a combination of (1) and (2) gives the n -related part of the free energy $\sim (\Delta/\lambda - T) n^2 + bn^4$, yielding a Néel temperature Δ/λ and $n \sim \sqrt{\Delta/\lambda - T}$ near the Néel temperature⁴⁰. The coupling energy E_c , the free energy difference under the two

conditions (Supplementary Section 15), is displayed in Fig.4(f), obtaining a correspondence of 0.01 meV(per unit cell) to the coupling field 0.86 T, which semi-quantitatively agrees with the experimental curves (≤ 200 K).

Discussion

Both experimental and theoretical results disclose that a small energy difference between the parallel and perpendicular states can be embodied as sizable interlayer coupling fields for the antiferromagnetic interlayer coupling owing to the vanishingly small moment, exhibiting unique advantage as compared with its ferromagnetic counterpart. A combination of the temperature and spacer thickness dependent SMR measurements, XMLD characterizations and the theory model demonstrates the orthogonal interlayer coupling in antiferromagnetic junctions.

In summary, the present discovery of strong orthogonal interlayer coupling in the all-antiferromagnetic junction exceeds the category of traditional collinear interlayer coupling, and is proposed to be mediated by quasi-long range order in spacer. Similar with the found of GMR in ferromagnets, such an orthogonal interlayer coupling in AFMs would hopefully serve as a promising basic building block for antiferromagnetic spintronics/magnonics and would be a significant step towards practical functional antiferromagnetic devices for data processing and storage with ultrahigh-density integration and ultrafast speed^{7,8}.

Methods

Sample preparations. The all-antiferromagnetic junctions $\text{Fe}_2\text{O}_3(12 \text{ nm})/\text{Cr}_2\text{O}_3(t \text{ nm})/\text{Fe}_2\text{O}_3(4 \text{ nm})$ ($t = 3.0, 3.5, 4.1, \text{ and } 4.4 \text{ nm}$) and control samples $\text{Fe}_2\text{O}_3(12 \text{ nm}), \text{Cr}_2\text{O}_3(4.4 \text{ nm})/\text{Fe}_2\text{O}_3(4 \text{ nm})$ were deposited on $\text{Al}_2\text{O}_3(0001)$ substrates in pulse laser deposition (PLD) system at 873 K, with a base vacuum of 1×10^{-8} torr. Then a 4 nm platinum layer was covered on the junctions by direct current sputtering at room temperature for spin Hall magnetoresistance (SMR) measurements to detect the orientation of Néel vectors. The highly insulating characteristic of samples is confirmed by resistivity measurements (Supplementary Note 1).

SMR measurements. The junctions were fabricated into Hall bars by standard photolithography combined with argon ion etching. A Keithley 2400 instrument provided a current I along the x -axis in the platinum for SMR measurements. A Keithley 2182 instrument was used to record the voltage along the platinum stripe during the magnetic field dependence of SMR measurement. The magnetic field (H) was applied along the same direction (along x -axis). The in-plane angle dependence of SMR is performed in a physical property measurement system (PPMS, Quantum Design).

XMLD measurements. X-ray magnetic linear dichroism (XMLD) spectra were carried out at Beamline 08U1A of the Shanghai Synchrotron Radiation Facility (SSRF). The x-ray absorption spectroscopy (XAS) data were obtained in total electron yield mode, which reflects the electronic structure of top Fe_2O_3 within

several nanometers, therefore the bottom Fe_2O_3 cannot contribute to XAS. A 2 nm-thick Pt capping layer was deposited on samples for electron conduction. The Fe *L*-edge XMLD spectra were obtained by the difference between linearly horizontal (//) and vertical (\perp) polarized XAS.

Declarations

Acknowledgments

We thank D. Z. Hou, R. Cheng, J. Xiao, X. G. Wan, K. Shen, Y. Z. Wu, and P. Yan for fruitful discussion. This work was supported by the National Key R&D Program of China (Grant No. 2017YFB0405704), the National Natural Science Foundation of China (Grant No. 51871130), and the Natural Science Foundation of Beijing, China (Grant No. JQ20010). We thank Beamline 08U1A of SSRF for XMLD measurements.

Author contributions

C. S. led the project. Y. Z. and C. S. proposed the study. Y. Z. prepared the samples and carried out the measurements with the help from H. B., M. Z., L. H., L. H., R. C. and Z. Z. L. L. and T. G. conducted theoretical analysis. Y. Z., L. L. and C. S. wrote the manuscript. All authors discussed the results and commented on the manuscript.

Competing interests: The authors declare no competing interests.

Data availability:

The data that support the findings of this study are available from the corresponding authors upon reasonable request.

References

1. Dieny, B. et al. Opportunities and challenges for spintronics in the microelectronics industry. *Nat. Electron.* **3**, 446–459 (2020).
2. Duine, R. A., Lee, K. J., Parkin, S. S. P. & Stiles, M. D. Synthetic Antiferromagnetic Spintronics. *Nat. Phys.* **14**, 217–219 (2018).
3. Baibich, M. N. et al. Giant magnetoresistance of (001)Fe/(001)Cr magnetic superlattices. *Phys. Rev. Lett.* **61**, 2472–2475 (1988).
4. Binasch, G., Grunberg, P., Saurenbach, F. & Zinn, W. Enhanced magnetoresistance in layered magnetic structures with antiferromagnetic interlayer exchange. *Phys. Rev. B* **39**, 4828–4830 (1989).
5. Parkin, S. S., More, N. & Roche, K. P. Oscillations in exchange coupling and magnetoresistance in metallic superlattice structures: Co/Ru, Co/Cr, and Fe/Cr. *Phys. Rev. Lett.* **64**, 2304–2307 (1990).
6. Jungwirth, T. et al. The multiple directions of antiferromagnetic spintronics. *Nat. Phys.* **14**, 200–203 (2018).

7. Jungwirth, T., Marti, X., Wadley, P. & Wunderlich, J. Antiferromagnetic spintronics. *Nat. Nanotechnol.* **11**, 231–241 (2016).
8. Baltz, V. et al. Antiferromagnetic spintronics. *Rev. Mod. Phys.* **90**, 015005 (2018).
9. Li, J. et al. Spin current from sub-terahertz-generated antiferromagnetic magnons. *Nature* **578**, 70–74 (2020).
10. Vaidya, P. et al. Subterahertz spin pumping from an insulating antiferromagnet. *Science* **368**, 160–165 (2020).
11. Qiu, H. et al. Ultrafast spin current generated from an antiferromagnet. *Nat. Phys.* **17**, 388–394 (2020).
12. Hortensius, J.R. et al. Coherent spin-wave transport in an antiferromagnet. *Nat. Phys.* (2021). <https://doi.org/10.1038/s41567-021-01290-4>.
13. Qiu, Z. et al. Spin colossal magnetoresistance in an antiferromagnetic insulator. *Nat. Mater.* **17**, 577–580 (2018).
14. Díaz-Guerra, C., Pérez, L., Piqueras, J. & Chioncel, M.F. Magnetic transitions in α -Fe₂O₃ nanowires. *J. Appl. Phys.* **106**, 104302 (2009).
15. Lebrun, R. et al. Long-distance spin-transport across the Morin phase transition up to room temperature in ultra-low damping single crystals of the antiferromagnet α -Fe₂O₃. *Nat. Commun.* **11**, 6332 (2020).
16. Han, J. et al. Birefringence-like spin transport via linearly polarized antiferromagnetic magnons. *Nat. Nanotechnol.* **15**, 563–568 (2020).
17. Hoogeboom, G. R., Aqeel, A., Kuschel, T., Palstra, T. T. M. & van Wees, B. J. Negative spin Hall magnetoresistance of Pt on the bulk easy-plane antiferromagnet NiO. *Appl. Phys. Lett.* **111**, 5 (2017).
18. Cheng, Y. et al. Anisotropic magnetoresistance and nontrivial spin Hall magnetoresistance in Pt/ α -Fe₂O₃ bilayers. *Phys. Rev. B* **100**, 220408 (2019).
19. Fischer, J. et al. Large spin Hall magnetoresistance in antiferromagnetic α -Fe₂O₃/Pt Heterostructures. *Phys. Rev. Appl.* **13**, 014019 (2020).
20. Ross, A. et al. Structural sensitivity of the spin Hall magnetoresistance in antiferromagnetic thin films. *Phys. Rev. B* **102**, 094415 (2020).
21. Zhou, Y.J. et al. A comparative study of spin Hall magnetoresistance in Fe₂O₃-based systems. *J. Appl. Phys.* **127**, 163904 (2020).
22. Park, B. G. et al. A spin-valve-like magnetoresistance of an antiferromagnet-based tunnel junction. *Nat. Mater.* **10**, 347–351 (2011).
23. Wadley, P. et al. Electrical switching of an antiferromagnet. *Science* **351**, 587–590 (2016).
24. Chen, X. et al. Electric field control of Neel spin-orbit torque in an antiferromagnet. *Nat. Mater.* **18**, 931–935 (2019).

25. Yan, H. et al. A piezoelectric, strain-controlled antiferromagnetic memory insensitive to magnetic fields. *Nat. Nanotechnol.* **14**, 131–136 (2019).
26. Tsai, H. et al. Electrical manipulation of a topological antiferromagnetic state. *Nature* **580**, 608–613 (2020).
27. Chumak, A.V., Vasyuchka, V.I., Serga, A.A. & Hillebrands, B. Magnon spintronics. *Nat. Phys.* **11**, 453–461 (2015).
28. Lebrun, R. et al. Tunable long-distance spin transport in a crystalline antiferromagnetic iron oxide. *Nature* **561**, 222–225 (2018).
29. Gomonay, O., Baltz, V., Brataas, A. & Tserkovnyak, Y. Antiferromagnetic spin textures and dynamics. *Nat. Phys.* **14**, 213–216 (2018).
30. Železný, J., Wadley, P., Olejník, K., Hoffmann, A. & Ohno, H. Spin transport and spin torque in antiferromagnetic devices. *Nat. Phys.* **14**, 220–228 (2018).
31. Dzyaloshinsky, I. A thermodynamic theory of “weak” ferromagnetism of antiferromagnetics. *J. Phys. Chem. Solids* **4**, 241–255 (1957).
32. Kuiper, P., Searle, B. G., Rudolf, P., Tjeng, L. H. & Chen, C. T. X-ray magnetic dichroism of antiferromagnet Fe₂O₃: The orientation of magnetic moments observed by Fe 2p x-ray absorption spectroscopy. *Phys. Rev. Lett.* **70**, 1549–1552 (1993).
33. Gota, S., Gautier-Soyer, M. & Sacchi, M. Magnetic properties of Fe₂O₃ (0001) thin layers studied by soft x-ray linear dichroism. *Phys. Rev. B* **64**, 224407 (2001).
34. Tobia, D., Winkler, E., Zysler, R. D., Granada, M. & Troiani, H. E. Size dependence of the magnetic properties of antiferromagnetic Cr₂O₃ nanoparticles. *Phys. Rev. B* **78**, 104412 (2008).
35. Wang, H., Du, C., Hammel, P. C., & Yang, F. Spin transport in antiferromagnetic insulators mediated by magnetic correlations. *Phys. Rev. B*, 91, 220410 (2015).
36. Dutta, P., Seehra, M. S., Thota, S., & Kumar, J. A comparative study of the magnetic properties of bulk and nanocrystalline Co₃O₄. *J. Phys.-Condes. Matter*, **20**, 015218 (2007).
37. Wang, H., Du, C., Hammel, P.C. & Yang, F. Antiferromagnonic spin transport from Y₃Fe₅O₁₂ into NiO. *Phys. Rev. Lett.* **113**, 097202 (2014).
38. Mermin, N.D. & Wagner, H. Absence of Ferromagnetism or Antiferromagnetism in One- or Two-Dimensional Isotropic Heisenberg Models. *Phys. Rev. Lett.* **17**, 1133–1136 (1966).
39. Stanley, H.E. & Kaplan, T.A. Possibility of a Phase Transition for the Two-Dimensional Heisenberg Model. *Phys. Rev. Lett.* **17**, 913–915 (1966).
40. Nagaosa, N. Quantum field theory in condensed matter physics. Springer Science & Business Media, 1999.

Figures

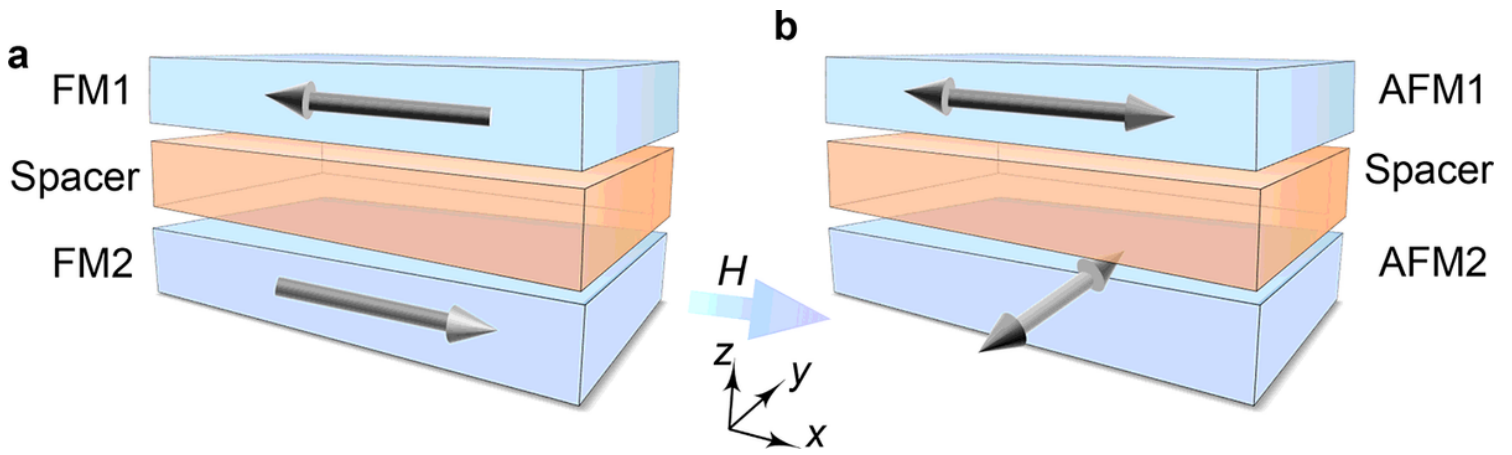


Figure 1

Two types of interlayer coupling in magnets. a, Illustration of the anti-parallel interlayer coupling in the top and bottom ferromagnetic layers (FM1 and FM2) b, Illustration of the orthogonal interlayer coupling between antiferromagnets (AFM1 and AFM2) found here.

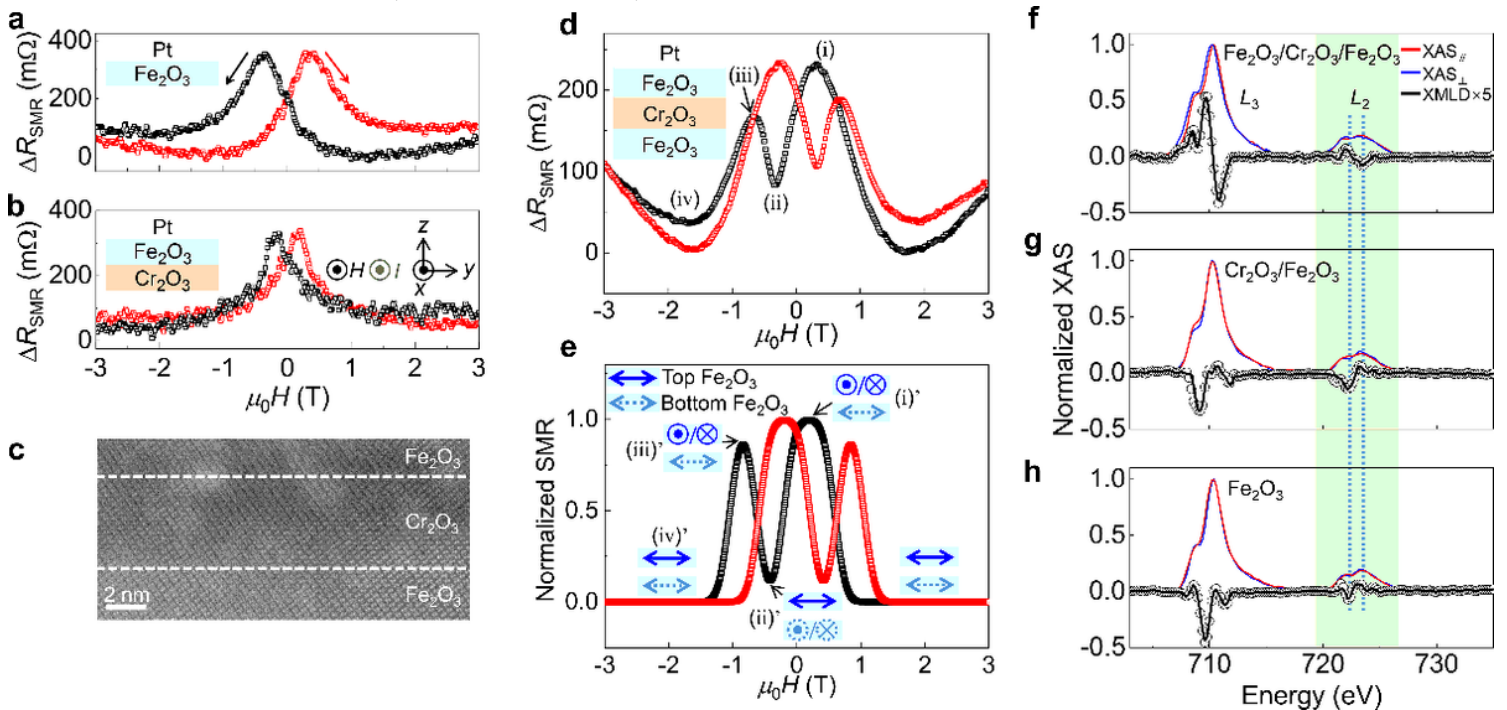


Figure 2

SMR and XMLD results of antiferromagnetic junctions. a,b, Magnetic field dependent SMR curves in control samples Fe₂O₃/Pt (a) and Cr₂O₃/Fe₂O₃/Pt (b) at 300 K. ΔR_{SMR} denotes the difference between resistance and the minimum. Inserts are experimental set-up. c, HAADF-STEM image of the Fe₂O₃/Cr₂O₃/Fe₂O₃ junction. d, SMR signals of Fe₂O₃/Cr₂O₃/Fe₂O₃/Pt samples at 300 K. e, Simulated SMR curve of Fe₂O₃/Cr₂O₃/Fe₂O₃/Pt samples at 300 K. Inserts are diagram of magnetic configurations at typical magnetic fields. f–h, Normalized XAS and XMLD spectra of Fe₂O₃/Cr₂O₃/Fe₂O₃ (f), Cr₂O₃/Fe₂O₃ (g) and Fe₂O₃ (h) samples. The XMLD spectra were taken from the differences of XAS spectra ($XAS_{\perp} - XAS_{\parallel}$) and then multiply by a factor of 5 at the absorption edges for clarity. The

highlighted region denotes Fe-L2 edge and the vertical dotted lines are guide for eyes to mark the valley and peak in XMLD curves.

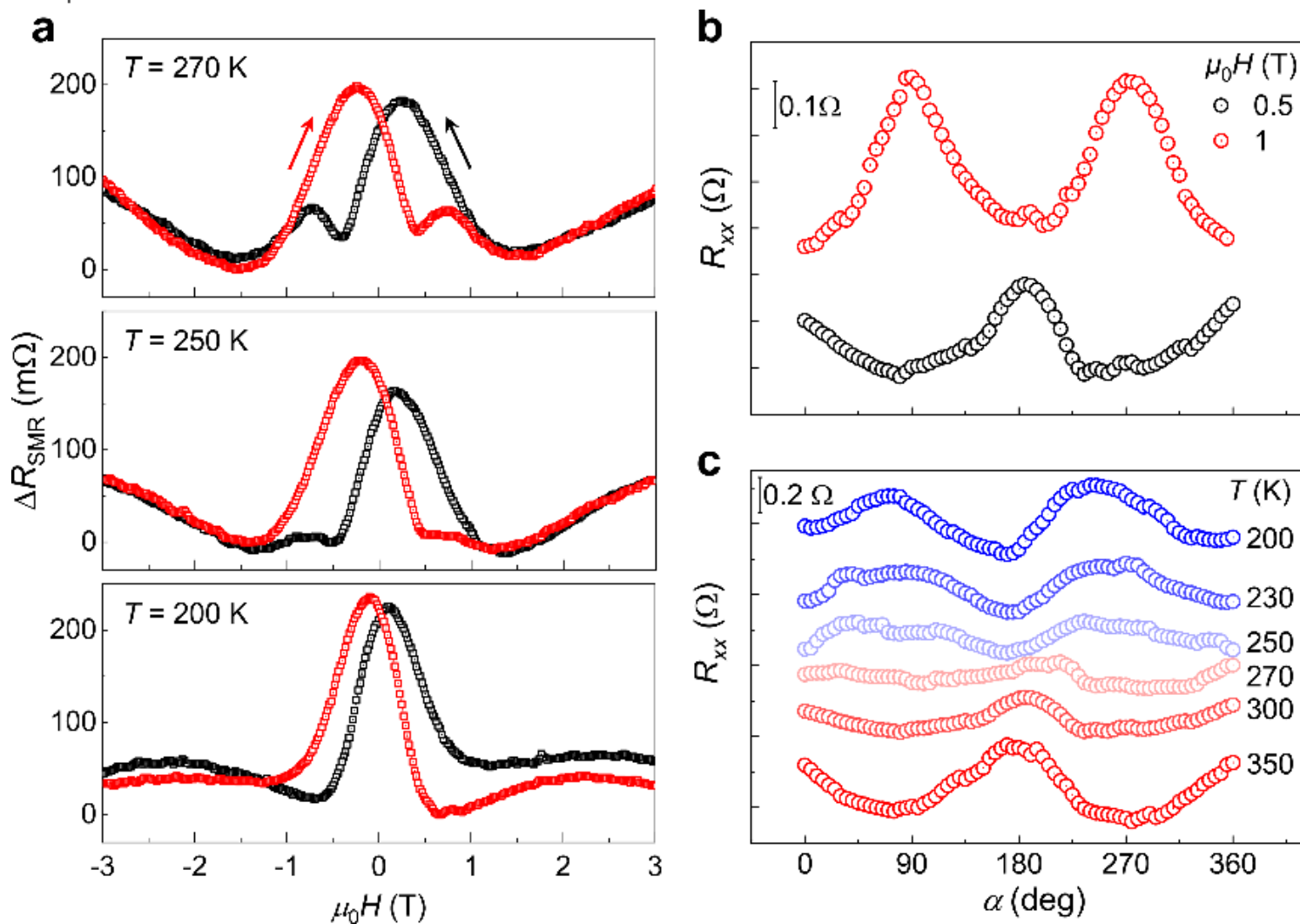


Figure 3

Temperature dependent SMR signals. a, SMR signals as a function of magnetic fields for the Fe2O3/Cr2O3/Fe2O3/Pt sample at various temperatures. b, Angle-dependence of SMR curves for the Fe2O3/Cr2O3/Fe2O3/Pt sample at $\mu_0 H = 0.5$ and 1 T. c, Corresponding SMR curves at various temperatures at $\mu_0 H = 0.5$ T. The curves are shifted vertically for clarity.

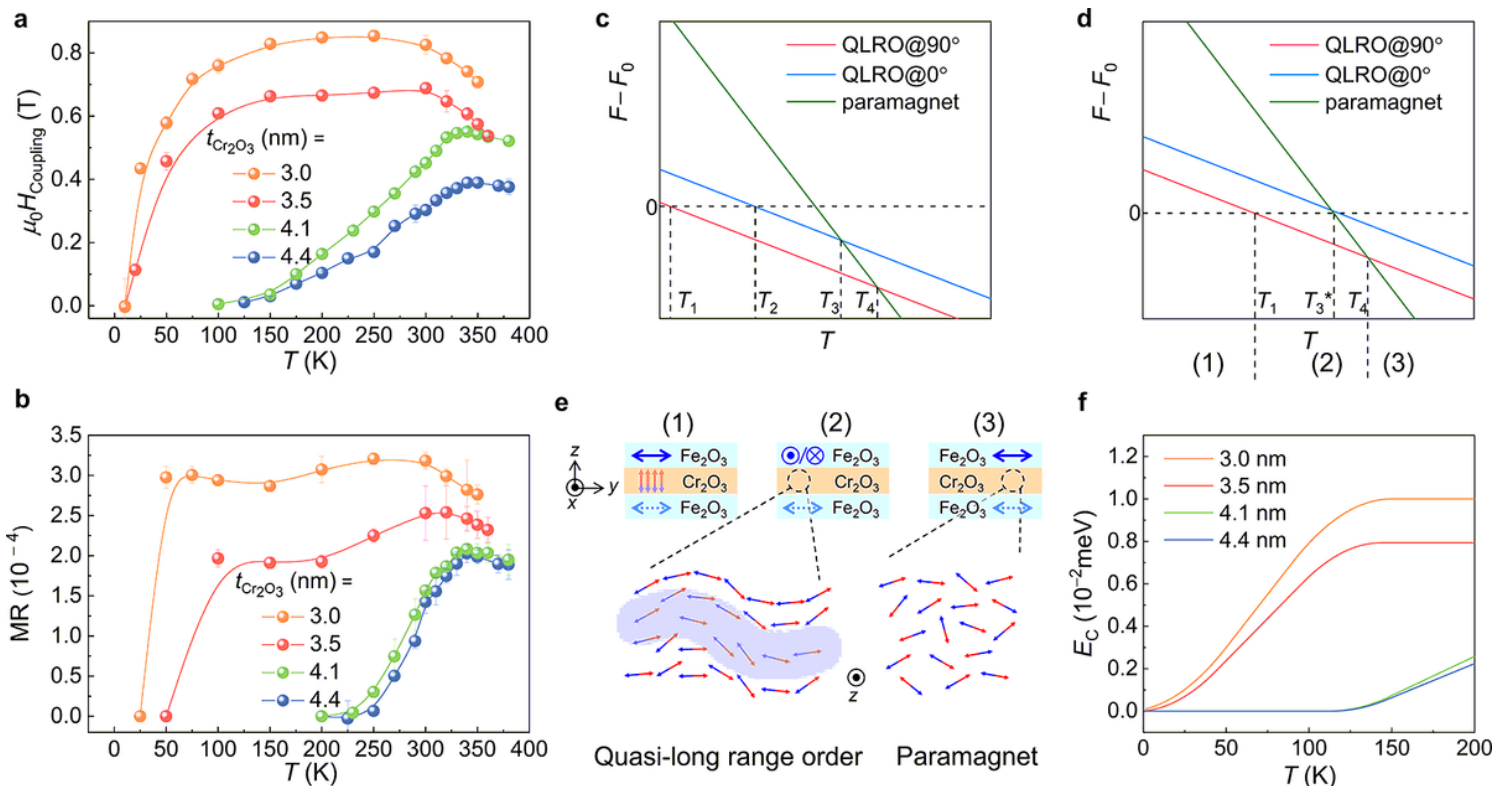


Figure 4

Temperature and spacer thickness dependent interlayer coupling. a, Summary of the location ($\mu_0 H_{\text{Coupling}}$) of the first peak for $\text{Fe}_2\text{O}_3/\text{Cr}_2\text{O}_3/\text{Fe}_2\text{O}_3/\text{Pt}$ samples with various Cr_2O_3 layer thicknesses ($t = 3.0, 3.5, 4.1,$ and 4.4 nm). b, Corresponding summary of the temperature-dependent magnetoresistance (MR). The error bars are estimated from the SMR data with sweeping H four times. c,d, Schematic free energy diagrams for the thin Cr_2O_3 (c) and the thick Cr_2O_3 (d) cases. e, Magnetic order in $\text{Fe}_2\text{O}_3/\text{Cr}_2\text{O}_3/\text{Fe}_2\text{O}_3$ at three temperature ranges (1)–(3) as marked in d. f, Temperature-dependence of calculated coupling energy.

Supplementary Files

This is a list of supplementary files associated with this preprint. Click to download.

- [ZhouAFMcouplingSupplementaryV120210930.docx](#)